

## Semi-empirical models of spicule from inversion of Ca II 8542 Å line

DAVID KURIDZE,<sup>1,2</sup> HECTOR SOCAS-NAVARRO,<sup>3,4</sup> JÚLIUS KOZA,<sup>5</sup> AND RAMON OLIVER<sup>6,7</sup>

<sup>1</sup>*Department of Physics, Aberystwyth University, Ceredigion, SY23 3BZ, UK*

<sup>2</sup>*Abastumani Astrophysical Observatory, Mount Kanobili, 0301, Abastumani, Georgia*

<sup>3</sup>*Instituto de Astrofísica de Canarias, 38205, C/Vía Láctea s/n, La Laguna, Tenerife, Spain*

<sup>4</sup>*Departamento de Astrofísica, Universidad de La Laguna, La Laguna, E-38205, Tenerife, Spain*

<sup>5</sup>*Astronomical Institute, Slovak Academy of Sciences, 059 60 Tatranská Lomnica, Slovakia*

<sup>6</sup>*Departament de Física, Universitat de les Illes Balears, E-07122 Palma de Mallorca, Spain*

<sup>7</sup>*Institute of Applied Computing & Community Code (IAC3), UIB, Spain*

(Received MM DD, 2020; Revised MM DD, 2020; Accepted MM DD, 2020)

### ABSTRACT

We study a solar spicule observed off-limb using high-resolution imaging spectroscopy in the Ca II 8542 Å line obtained with the CRisp Imaging SpectroPolarimeter (CRISP) on the Swedish 1-m Solar Telescope. Using a new version of the non-LTE code NICOLE specifically developed for this problem we invert the spicule single- and double-peak line profiles. This new version considers off-limb geometry and computes atomic populations by solving the 1D radiative transfer assuming a vertical stratification. The inversion proceeds by fitting the observed spectral profiles at 14 different heights with synthetic profiles computed in the model by solving the radiative transfer problem along its length. Motivated by the appearance of double-peak Ca II 8542 Å spicule profiles, which exhibit two distinct emission features well separated in wavelength, we adopt a double-component scenario. We start from the ansatz that the spicule parameters are practically constant along the spicule axis for each component, except for a density drop. Our results support this ansatz by attaining very good fits to the entire set of  $14 \times 4$  profiles (14 heights and 4 times). We show that the double-component model with uniform temperature of 9 560 K, exponential decrease of density with a height scale of 1 000 – 2 000 km, and the counter-oriented line-of-sight velocities of components reproduce the double-peak line profiles at all spicule segments well. Analyses of the numerical response function reveals the necessity of the inversions of spectra at multiple height positions to obtain height-dependent, degeneracy-free reliable model with a limited number of free parameters.

*Keywords:* Solar chromosphere; Solar spicules; Spectroscopy; Radiative transfer simulations

### 1. INTRODUCTION

Spicules are small-scale, jet-like plasma features observed ubiquitously at the solar limb and have been reviewed by Beckers (1968, 1972), Sterling (2000), and Tsiropoula et al. (2012). Originating in the active regions and network boundaries, they protrude into the corona and can act as conduits channeling energy and mass from the solar photosphere into the upper layers. Despite tremendous observational and theoretical efforts since their discovery in the 19th century (Secchi 1875), many aspects of spicule physics, such as their formation mechanism, magnetism, and thermodynamic properties remain the central subject of ongoing solar research.

There is a wide variety of spicular jets in the solar atmosphere observed in strong chromospheric lines. Their classification is based on their morphological properties. However, there is no final consensus regarding their categorization. A traditional spicule is defined as a chromospheric jet with height between 6 500 and 9 500 km, width between 700 – 2 500 km and lifetime of up to 10 – 15 minutes (Beckers 1972; Pasachoff et al. 2009). They are charac-

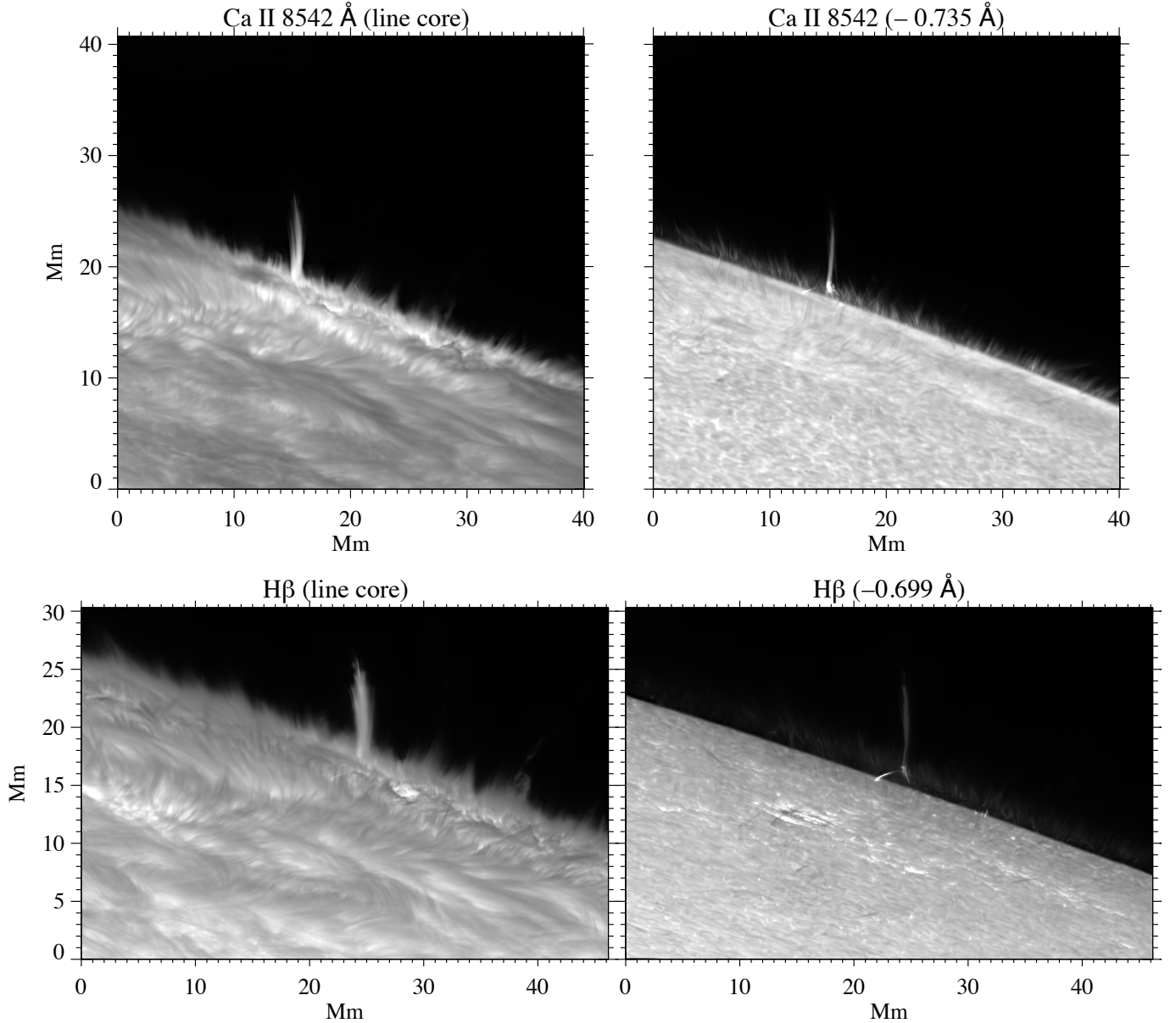


**Figure 1.** Overview of SST observations of the spicule on 2018 June 22 at 08:34:27 UT at the western limb near AR NOAA 12714. Each image is byte-scaled independently. Top: CRISP Ca II 8542 Å line core image (left) and blue wing image at  $\Delta\lambda = -0.735$  Å (right). Bottom: CHROMIS H $\beta$  line core image (left) and blue wing image at  $\Delta\lambda = -0.699$  Å (right).

terized by rising and falling motions with speeds of  $\sim 20 - 40 \text{ km s}^{-1}$ . Disk observations have revealed similar types of chromospheric fine structures such as quiet Sun mottles (Suematsu et al. 1995) and active region dynamic fibrils (De Pontieu et al. 2004; Hansteen et al. 2006). At the limb de Pontieu et al. (2007) discovered energetic and short-lived spicular features called type II spicules. Soon after, structures with similar properties were identified in high resolution ground-based observations on the solar disk. These absorption features detected in the blue and red wings of the Ca II and H $\alpha$  lines are called rapid red-shifted and blue-shifted excursions (Langangen et al. 2008; Rouppe van der Voort et al. 2009; Kuridze et al. 2015a).

Spicular structures are often observed with inverted Y-shaped footpoints both at the limb and on the disk (Yokoyama & Shibata 1995; Shibata et al. 2007; He et al. 2009; Morita et al. 2010; Nishizuka et al. 2011; Nelson et al. 2019). Due to their similarity with coronal X-ray jets, Yokoyama & Shibata (1995) and Shibata et al. (2007) refer to them

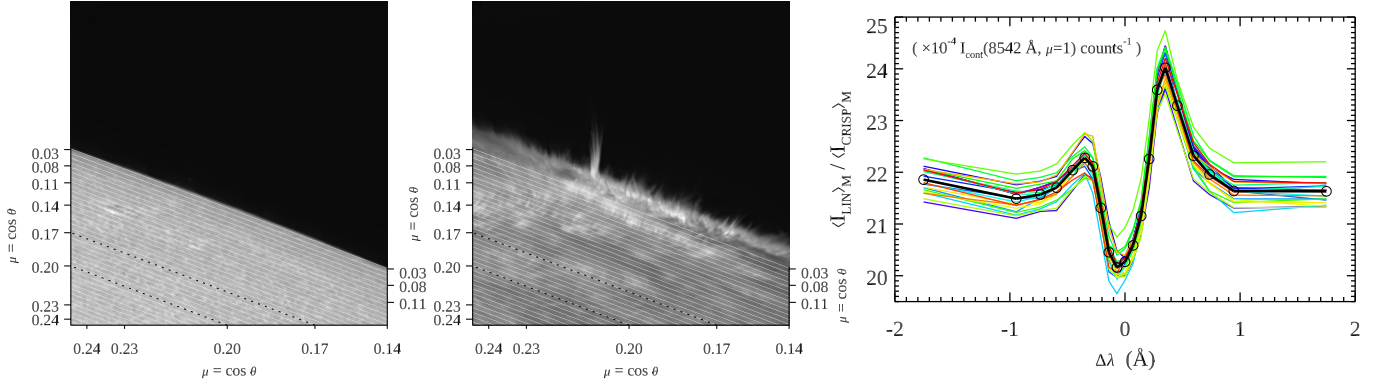


**Figure 2.** Radiometric calibration of SST/CRISP Ca II 8542 Å data. Composite of Ca II wing images at  $\Delta\lambda = \pm 1.75$  Å (left) and line core image (middle) at 08:32:38 UT. The mesh of white lines marks a sample of pixel lines labeled with the direction cosines  $\mu = \cos\theta$  and used for computing radial intensity gradient. The black dotted lines define the area and the range of  $\mu \in (0.17, 0.20) \equiv M$  adopted for computing the calibration profiles in the right panel. Right: Calibration profiles. Rainbow colors illustrate times of individual SST/CRISP scans. Blue, yellow, and red correspond to start, middle, and end of observations. The black curve is an average of the profiles. The black circles indicate the wavelength sampling of the observed Ca II profile.

as anemone jets. The topology of these jets suggests that they are formed as a result of magnetic reconnection in the lower solar atmosphere.

A reliable quantitative measurement of the physical parameters in spicules is extremely challenging. The difficulties arise due to the fact that they are very dynamic features, with spatial and temporal scales that are often close to the resolution limit of modern solar telescopes and the large number of spicules in the solar atmosphere makes overlapping emissions coming from them difficult to separate. Chromospheric spectral lines are sensitive to plasma properties in spicules. Therefore, chromospheric spectroscopy offers the most powerful diagnostic opportunities. However, modeling and interpretation of chromospheric spectral lines are always challenging as they require solving the complex non-LTE (i.e., departures from Local Thermodynamic Equilibrium) radiative transfer problem.

It is widely accepted that the external radiation field irradiating spicules is entirely photospheric (Beckers 1968) and their emission in most chromospheric lines forms under strong non-LTE conditions. The line profiles of spicules in the strong chromospheric spectral lines of hydrogen Balmer series, single ionized calcium lines, and helium lines appear in emission with central reversal and broad, enhanced, asymmetric wings very often (Beck et al. 2016). As discussed by Beckers (1972) and confirmed by subsequent studies, the central reversals in spicule spectra are not produced by the reduction of the source function at the line core (self-absorption), but rather related to their non-thermal dynamics.

One of the first spectroscopic diagnostics of spicule parameters was carried out by Beckers (1968). He assumed that the spicule is a cylinder with the diameter of 815 km situated vertically on the Sun and irradiated by solar radiation. Theoretical relations between electron temperature  $T_e$  and electron densities  $n_e$  were calculated for the intensities of H $\alpha$ , Ca II, and He spectral lines through solving the radiative transfer equation and the statistical equilibrium equation in non-LTE. Then, for the observed intensities at different heights along spicules,  $T_e - n_e$  curves were obtained and interceptions between these curves for different lines were used for diagnostics of temperature and electron density. The temperature of the spicules reported by Beckers (1968) between the heights of 2 – 8 Mm is  $\sim 9000 - 16000$  K and the electron densities between 4 – 8 Mm are  $1.5 \times 10^{11} - 4.3 \times 10^{10} \text{ cm}^{-3}$ . Alissandrakis (1973) and Krall et al. (1976) implemented the same method and obtained similar results for electron density and temperature as Beckers (1968). Socas-Navarro & Elmore (2005) used multiline full Stokes observations of spicules in the Ca II 8498, 8542 Å, and He I 10830 Å lines to derive spicule properties. They found that the Ca II and He I 10830 Å lines have almost identical widths suggesting that most of the broadening in spicules are non-thermal, which in turn indicates that the electron temperature of the spicule should be lower than 13000 K. Measurements of magnetic fields in spicules using spectropolarimetric single-line observations have been done in the He I 10830 Å line (Trujillo Bueno et al. 2005; Centeno et al. 2010; Orozco Suárez et al. 2015), in the Ca II 8542 Å line (Kriginsky et al. 2020), and in the He I 5876 Å (D3) line (López Ariste & Casini 2005; Ramelli et al. 2005, 2006). For more details on spicule spectropolarimetry see Trujillo Bueno (2010).

To interpret the spectra of spicular structures observed against the solar disk and appearing as absorbing features in chromospheric lines, Beckers (1964) developed a different method known as the "cloud model". The cloud model is a simple inversion technique that fits the observed intensity contrast profile with four free parameters — the source function, the optical depth, the Doppler width, and the Doppler shift. With these parameters one can determine several other physical parameters of the structure. This method has been successfully applied over the years to chromospheric structures observed in H $\alpha$  (Alissandrakis et al. 1990; Tsiropoula & Schmieder 1997; Tziotziou et al. 2003).

Since the launch of the *Interface Region Imaging Spectrograph* (IRIS; De Pontieu et al. 2014), spicules have been intensively observed and investigated in several UV lines by Pereira et al. (2014) and Skogsrud et al. (2015). Alissandrakis et al. (2018) compared the Mg II k and h line profiles observed with IRIS with computations from a 1D non-LTE model and estimated the temperature and electron density from the lower to the upper part of spicules to be between  $\sim 8\,000 - 20\,000$  K and  $1.1 \times 10^{11} - 4 \times 10^{10}$  cm $^{-3}$ , respectively. More recently, Tei et al. (2020) used 1D non-LTE vertical slab models in single- and multiple slab configurations and concluded that the width of the Mg II k and h line profiles can be significantly influenced by a superposition of multiple spicules along the LoS.

An alternative method of plasma diagnostics in spicules is the so-called magnetoseismology, which relies on observations of magnetohydrodynamic waves to infer the properties of a magnetic flux tube (Zaqarashvili et al. 2007; Zaqarashvili & Erdélyi 2009; Verth et al. 2011; Kuridze et al. 2013; Morton 2014). These methods also depend on the assumed nature of the wave modes (local tube modes versus genuine Alfvén waves in more homogeneous media).

Spicule temperature and density were also determined using radio data obtained with the Atacama Large Millimeter/submillimeter Array (ALMA; Wootten & Thompson 2009) radio telescope by Shimojo et al. (2020). They derived kinetic temperature and the number density of ionized hydrogen in the spicule plasma seen in the ALMA 100 GHz images as 6800 K and  $2.2 \times 10^{10}$  cm $^{-3}$ .

The vertical stratification of the physical parameters along chromospheric structures can be obtained using semi-empirical models that attempt to reproduce the observed profiles in non-LTE radiative transfer. A powerful way to construct atmospheric models with a semi-empirical approach is to fit the observed Stokes profiles using inversion algorithms (de la Cruz Rodríguez & van Noort 2017). Through such inversions, the ionization equilibrium, statistical equilibrium, and radiative transfer equations are solved numerically to synthesize the Stokes profiles under a set of predefined initial atmospheric conditions. The Ca II infrared (IR) triplet line at 8542 Å is well suited for the development of such models due to its sensitivity to physical parameters in the solar photosphere and chromosphere (Pietarila et al. 2007; Cauzzi et al. 2008). Furthermore, calcium is singly ionized under typical chromospheric conditions, with negligible partial redistribution effects for the Ca II IR lines (Uitenbroek 1989), making their modeling and interpretation of the observations more straightforward. The non-LTE radiative transfer code NICOLE (Socas-Navarro et al. 2000, 2015) is a suitable tool for our purposes here since it allows for the synthesis and inversion of Ca II Stokes profiles and the construction of semi-empirical models. Inversions with NICOLE have been successfully applied to the study of spectropolarimetric Ca II 8542 Å observations of umbral flashes in sunspots (de la Cruz Rodríguez et al. 2013), granular-sized magnetic elements (magnetic bubbles) in an active region (de la Cruz Rodríguez et al. 2015), and chromospheric flares (Kuridze et al. 2017, 2018). However, NICOLE was not designed to work on off-limb spectroscopic observations as it assumes a geometry in which the emergent radiation comes from the bottom of the atmosphere and hydrostatic equilibrium is imposed at each inversion iteration to compute the plasma density and pressure.

In this paper we use a new version of NICOLE to invert high-resolution imaging spectroscopy in the Ca II 8542 Å line to construct models of the solar off-limb spicule (Figure 1). This new version first computes the atomic level populations in a vertically stratified atmosphere, including the spicule up to 10 Mm. Then, once all the source functions and opacities are known, a final formal solution computes the spectra in the direction of the line of sight, which in this case is horizontal, at a discrete set of heights specified by the user (in our case, the 14 points where observed spectra are available). These 14 profiles are fitted simultaneously with one single model atmosphere. The model has two components, as explained below. The chosen parameterization allows us to retrieve the height stratification of temperature, mass and electron density, LoS velocity, and optical thickness along the spicule.

## 2. OBSERVATIONS AND DATA REDUCTION

### 2.1. Observational setup

We observed the west limb of the Sun between 08:20 and 08:43 UT on 2018 June 22 near the active region (AR) NOAA 12714. The heliocentric coordinates of the center of the field of view (FoV) at the beginning of the observations were [937'', 127'']. Observations were made with the CRisp Imaging SpectroPolarimeter (CRISP; Scharmer 2006;

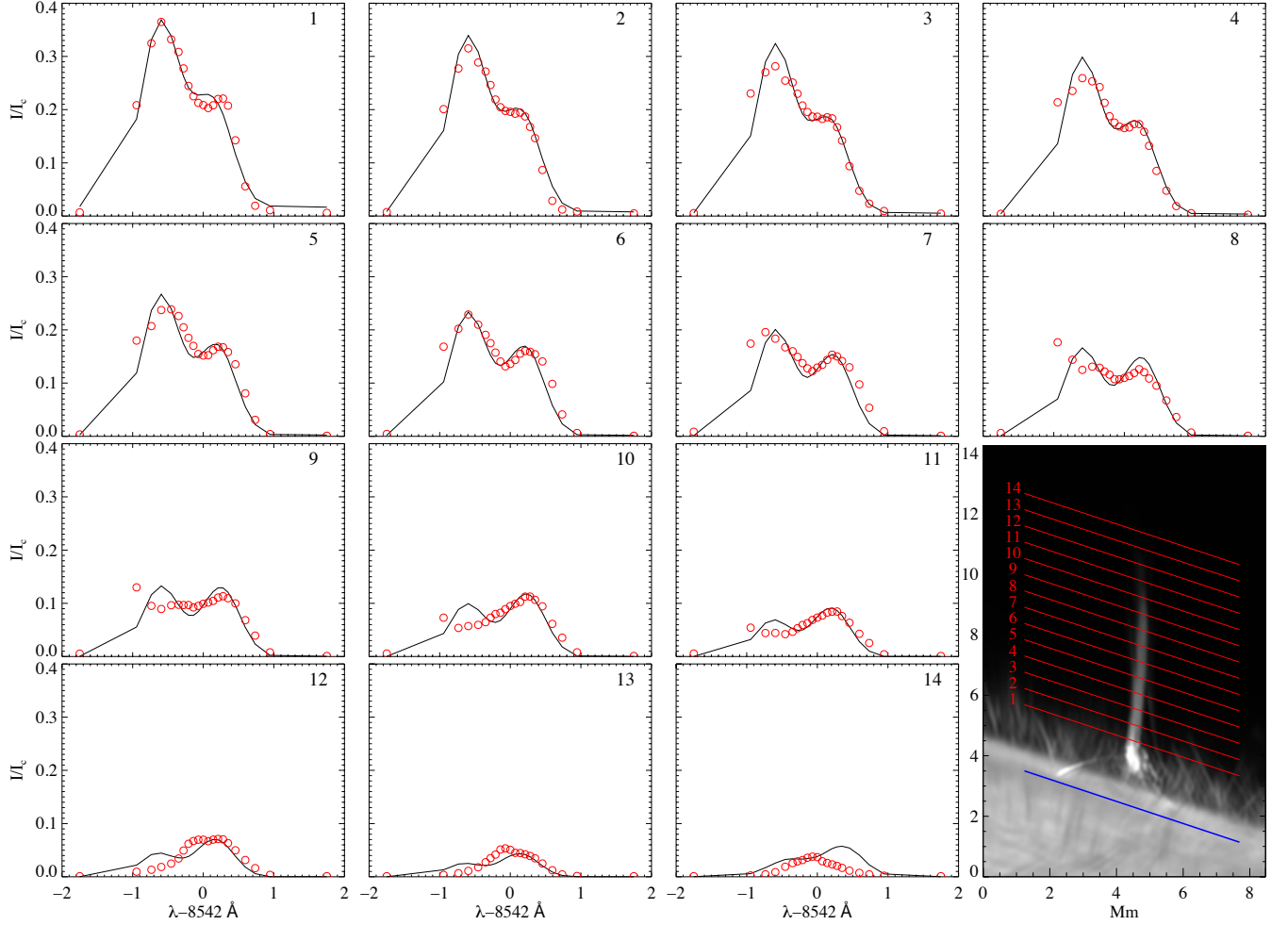


**Figure 3.** Observed (red circles) and best-fit synthetic (solid black lines) Ca II 8542 Å line profiles of the spicule at fourteen different positions along its axis at 08:34:27 UT. The numbers from 1 (spicule footpoint) to 14 (spicule top) in the top right corners indicate the heights at which the line profiles along the spicule (bottom right panel) are located. The intensity of line profiles is normalized to the quiet Sun continuum intensity  $I_c$  at 8542 Å in the disk center. Bottom right: The spicule in the blue wing of Ca II 8542 Å at  $\Delta\lambda = -0.735$  Å. The red lines identify the heights of origin of the spicule profiles 1 – 14. The blue line shows the location of the photosphere at  $\tau_{5000} = 1$  at  $\mu = 1$ . The tickmarks of  $y$  axis are labeled in Mm.

Scharmer et al. 2008) and the CHROMospheric Imaging Spectrometer (CHROMIS) instruments, both based on dual Fabry-Pérot interferometers (FPI) mounted on SST. The imaging setup includes a dichroic beamsplitter with the transmission/reflection edge at 5000 Å. CRISP is mounted in the reflected red beam and CHROMIS in the transmitted blue beam (Löfdahl et al. 2018, Figure 2).

The CRISP data comprises narrow-band imaging spectropolarimetry in the Ca II 8542 Å line profile sampled from  $-1.75$  Å to  $+1.75$  Å in 21 line positions  $\pm 1.75$ ,  $\pm 0.945$ ,  $\pm 0.735$ ,  $\pm 0.595$ ,  $\pm 0.455$ ,  $\pm 0.35$ ,  $\pm 0.28$ ,  $\pm 0.21$ ,  $\pm 0.14$ ,  $\pm 0.07$ ,  $0.0$  Å from the line center (hereafter, unless specified otherwise, when referring to the Ca II line we mean the Ca II 8542 Å line). Each spectral scan of the Ca II line had an acquisition time of 16 s but the cadence of the CRISP time series was 33 s due to the inclusion of spectropolarimetric scans in the Fe I 6302 Å photospheric line. However, we note that the present paper includes only the analysis of the Ca II data, as the spicule analyzed in this study and its footpoints were not detected in the Fe I line. The CRISP data are processed by the CRISPRED reduction pipeline (de la Cruz Rodríguez et al. 2015) and reconstructed with Multi-Object Multi-Frame Blind Deconvolution (MOMFBD; Löfdahl 2002; van Noort et al. 2005).

Simultaneous observations were taken with the CHROMIS imaging spectrometer – a dual FPI observing in the range of 3900 – 4900 Å. The CHROMIS observations comprise narrow-band and wide-band spectral imaging in the



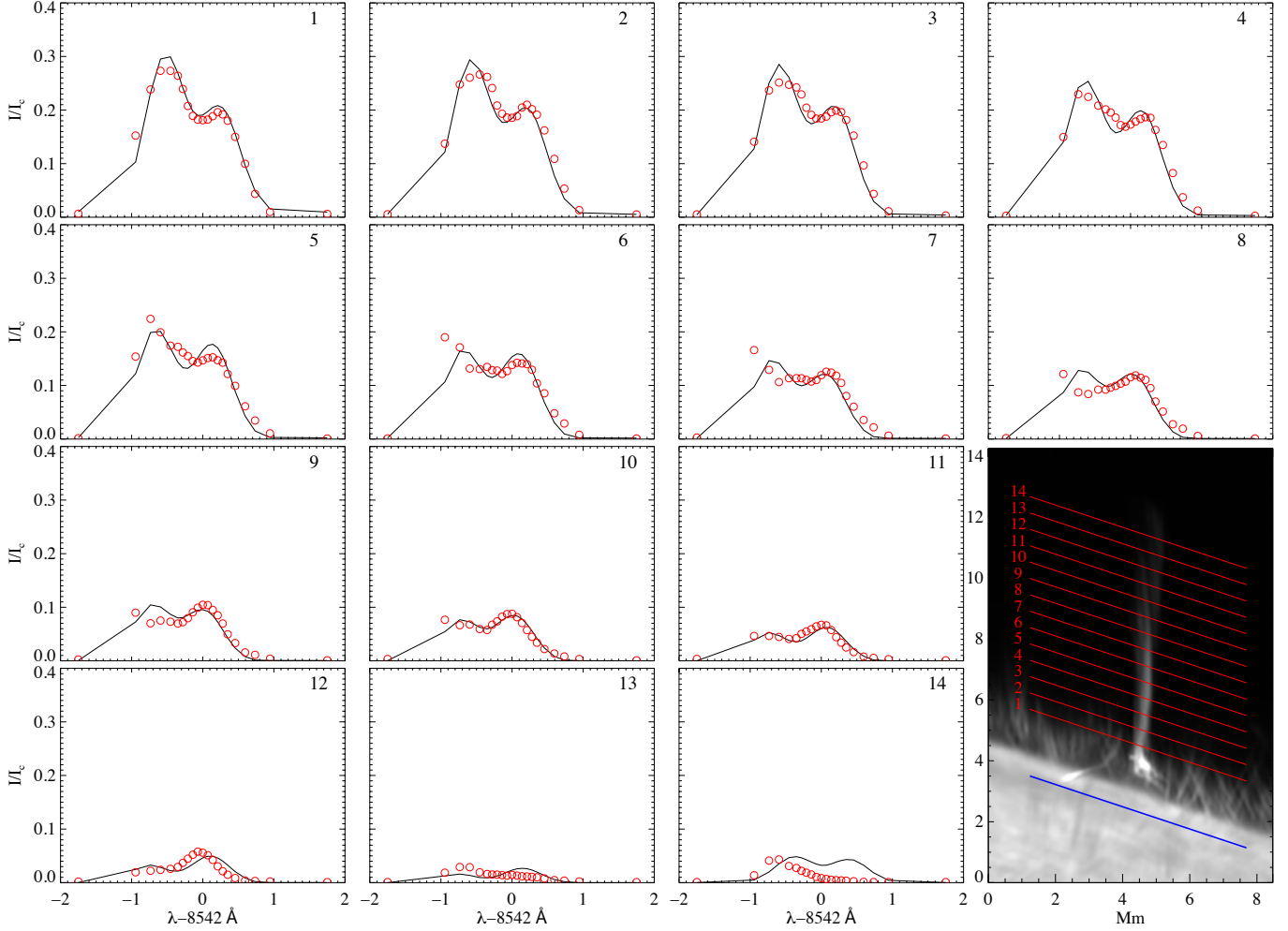


Figure 4. Same as Figure 3 but at 08:35:33 UT.

H $\beta$  and Ca II H 3968.5 Å lines, plus one position in the continuum at 4000 Å. CHROMIS data are processed using the CHROMISRED reduction pipeline, which includes MOMFBD image restoration (Löfdahl et al. 2018).

In this work we focus only on the inversion of the CRISP Ca II Stokes  $I$  profiles.

## 2.2. Data Radiometric Calibration

The inversion of SST/CRISP spectroscopic observations of the spicule requires careful intensity calibration of the data. Inversion codes, including NICOLE, usually require the input data to be calibrated with respect to the quiet-Sun continuum intensity at the disk center to convert the digital counts in the observations to actual physical units. However, this was not an option in our case due to the absence of a disk-center continuum reference in the data.

To calibrate a single CRISP Ca II scan, the Stokes  $I$  wing images at  $\Delta\lambda = \pm 1.75$  Å are averaged yielding a composite image (Figure 2: left panel). The limb is identified in the composite image by the IDL function `sobel.pro` and approximated by a limb line. Then a dense mesh of 536 lines parallel to the limb is created covering the whole visible disk. Using the solar disk radius of  $944''338$  and the CRISP spatial sampling of  $0''.057 \text{ pixel}^{-1}$  the position cosines  $\mu = \cos\theta$  corresponding to the mesh lines are calculated. A sample of 38 equidistant mesh lines and the position cosines are shown in Figure 2 (left and middle panel). Averaging Stokes  $I$  pixel intensities over particular mesh lines at a given  $\mu$  yields radial intensity gradients  $I_{\text{CRISP}}(\lambda_{\text{CRISP}}, \mu)$  at particular CRISP wavelengths,  $\lambda_{\text{CRISP}}$ . Quasi-linear intensity segments  $I_{\text{CRISP}}(\lambda_{\text{CRISP}}, M)$  (not shown here) in the position cosines ranging from 0.17 to 0.20 (hereafter  $M \equiv \mu \in (0.17, 0.20)$ ) are adopted for calibration, avoiding the remnant of the AR NOAA 12714 seen at  $\mu \sim 0.13$  (Figure 1: bottom right panel and Figure 2: left panel). The calibrated Ca II profiles from Linsky et al. (1970) are adopted as a reference extrapolating them for  $M$  and convolving them with the transmission profile of

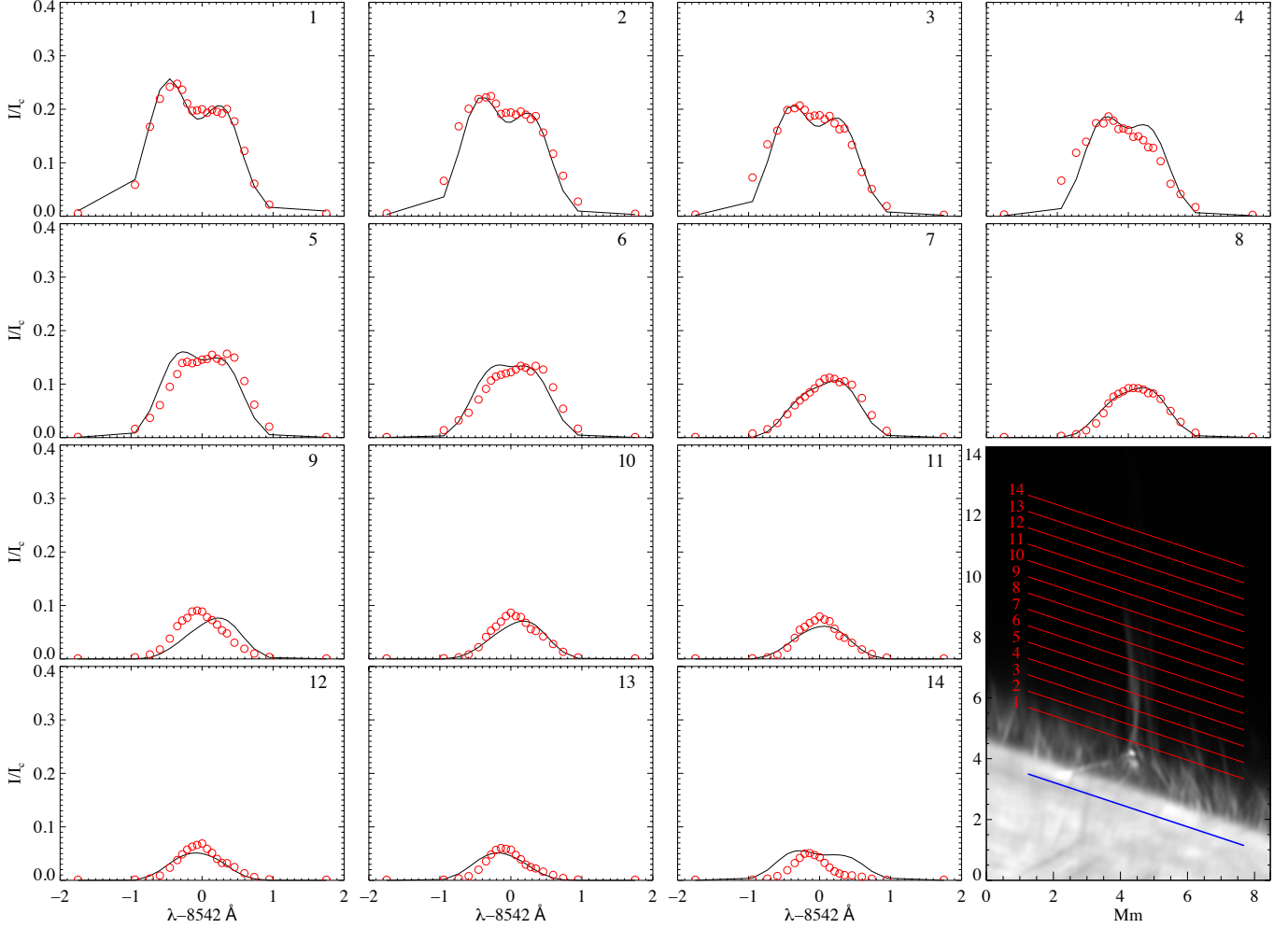


**Figure 5.** Same as Figure 3 but at 08:38:18 UT.

the CRISP Fabry-Pérot etalons provided by J. de la Cruz Rodríguez (2017, private communication). The resulting profiles are referred to hereafter as  $I_{\text{LIN}}(\lambda_{\text{LIN}}, M)$ . To compensate for differences between the CRISP wavelength scale  $\lambda_{\text{CRISP}}$  and the scale  $\lambda_{\text{LIN}}$  used in Linsky et al. (1970), the precise line minimum positions  $\lambda_c$  of  $I_{\text{CRISP}}(\lambda_{\text{CRISP}}, \mu)$  are measured in a broad range of  $\mu$  values. Then the profile minimum positions of  $I_{\text{LIN}}(\lambda_{\text{LIN}}, M)$  are compared to  $\lambda_c$  at the corresponding  $\mu$ , allowing the interpolation of  $I_{\text{LIN}}(\lambda_{\text{LIN}}, M)$  on the CRISP wavelength scale. This yields the reference intensity gradients  $I_{\text{LIN}}(\lambda_{\text{CRISP}}, M)$ . The ratio of the reference intensity gradient  $\langle I_{\text{LIN}}(\lambda_{\text{CRISP}}, M) \rangle_M$  and the observed gradient  $\langle I_{\text{CRISP}}(\lambda_{\text{CRISP}}, M) \rangle_M$ , averaged over the  $M$  range, renders a calibration profile (Figure 2: right panel) allowing the conversion of the Ca II Stokes  $I$  intensities from digital numbers to the physical units expressed relative to the quiet Sun continuum intensity at 8542 Å in the disk center  $I_c$  (Figures 3 – 6). To compensate for possible variations in sky transparency, the calibration procedure is repeated separately for each CRISP scan. The right panel of Figure 2 shows a cluster of profiles used for calibrating particular scans.

### 2.3. Corrections for canopy emission and stray light

We subtracted two non-spicular components from the spicule spectra – average foreground canopy emission and off-limb stray light. The height of the chromospheric canopy, populated by short type II spicules and the background chromosphere, was estimated as  $\sim 2800$  km above the photospheric limb by the Ca II line center images. Then the reference canopy Ca II profiles  $I_{\text{ref}}(h, \lambda)$  were created for each height  $h$  between the photospheric limb and the top of the canopy. Assuming that only foreground canopy emission contributes to the spicule emission, the intensity  $0.5I_{\text{ref}}(h, \lambda)$  was subtracted from the spicule profile at the same height between the photospheric limb and the canopy top. Above the canopy, the stray light intensity  $I_{\text{stray}}(h, \lambda)$  was determined by intensity gradients at particular heights

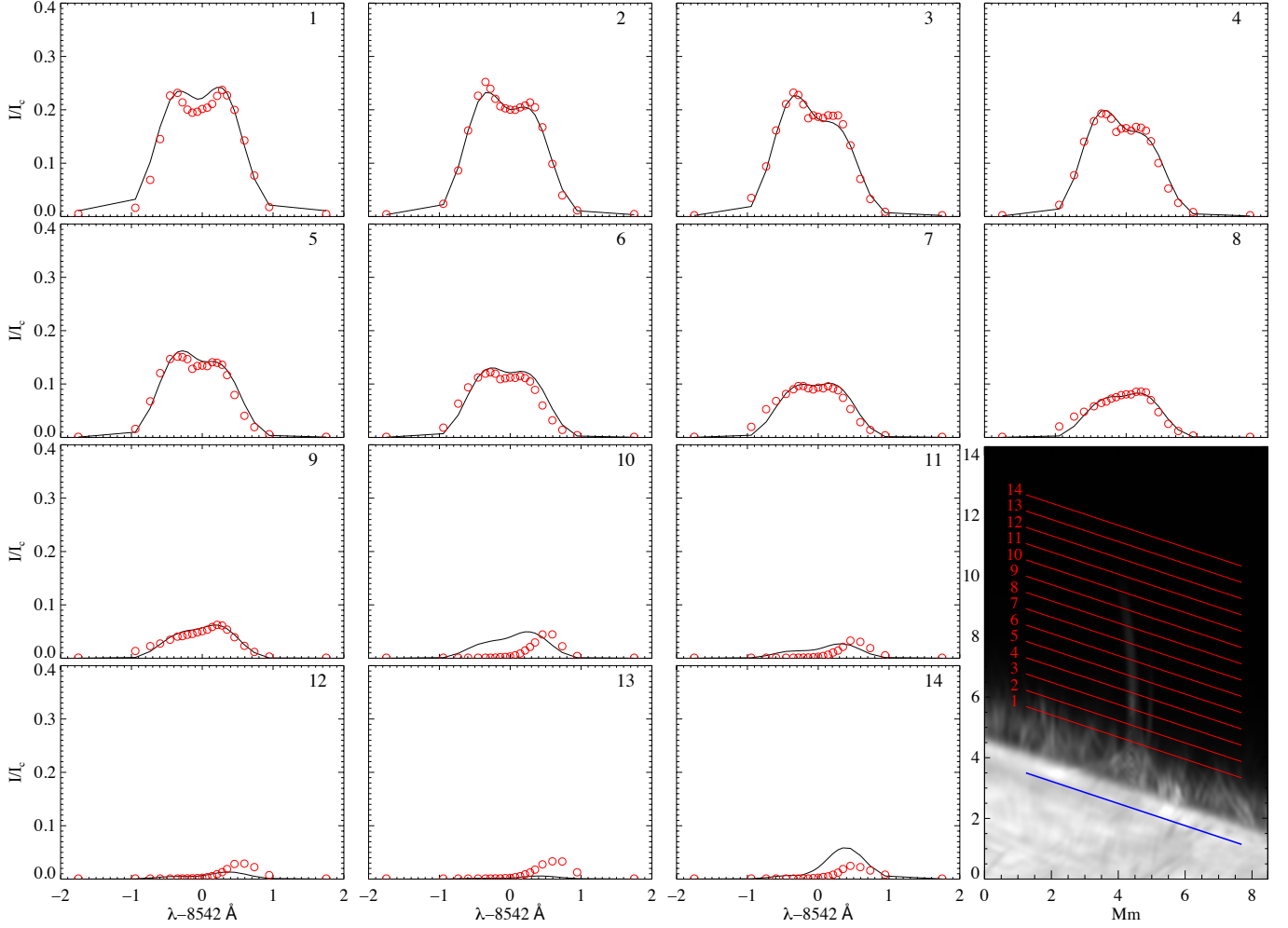


**Figure 6.** Same as Figure 3 but at 08:41:03 UT.

and wavelengths and subtracted from the spicule profiles at the same heights. We note that the canopy and stray-light emissions are significantly weaker compared to the emission that comes from the spicule due to its exceptional brightness and clear separation. Therefore, the subtractions modify the spicule spectra only slightly.

### 3. SPICULE APPEARANCE AND LINE PROFILES

Figure 1 shows images of the spicule in the Ca II and H $\beta$  line core and blue wing images taken at 08:34 UT. The spicule was already developed at the start of the observations at  $\sim 08:20$  UT and disappeared after around 20 minutes. The line core images show that the structure extends up to the height  $\sim 9$  Mm above the limb, well above the chromospheric canopy populated with shorter type II spicules (Figure 1). The blue wing images nicely illustrate the spicule footpoint shaped as the inverted Y. It suggests an association of the spicule with small-scale magnetic reconnection, which likely launched the spicule. Thus the event discussed here is of the same type and origin as those in Shibata et al. (2007), He et al. (2009), Nishizuka et al. (2011), and Nelson et al. (2019). The spicule has an inclination angle  $\theta \sim 70^\circ$  with respect to the limb. The average width of the spicule is around 1 Mm.

We select four line profile scans taken at  $\sim 08:34$ ,  $08:35$ ,  $08:38$ , and  $08:41$  UT when the spicule was relatively bright and started becoming fainter. The red circles in Figures 3 – 6 represent the observed Ca II line intensities of the spicule for the four selected snapshots at fourteen space-separated positions along its axis. They are normalized with respect to the quiet-Sun continuum intensity at  $8542 \text{ \AA}$ ,  $\mu = 1$ )  $\equiv I_c$ . The red lines in the lower right panels of Figures 3 – 6 show the equidistant heights located at different positions along the spicule. Along each height the pixel with maximum wavelength integrated intensity are found and line profiles for those pixels are selected for inversions. The lowest (1) and highest (14) positions (the lower right panels in Figures 3 – 6) are located at the



heights  $\sim 2050$  and  $8600$  km above the limb, respectively. It is known that the limb is uplifted by about  $\sim 350$  km above the base of the photosphere at  $\tau_{5000} = 1$  measured at  $\mu = 1$  (Lites 1983, Table 1). This off-set is due to an increase of optical depth at  $5000 \text{ \AA}$  when looking from disk center ( $\mu = 1$ ) to limb ( $\mu = 0$ ). The edge of the solar disk at the Ca II  $\pm 1.75 \text{ \AA}$  line positions is also expected to be formed at  $\sim 350$  km above the  $\tau_{5000} = 1$  at  $\mu = 1$ . The blue lines in the lower right panel of Figures 3 – 6 show the location of the true photosphere and the indicated heights of the selected pixels along the spicule are considered as a projection on the normal to the photospheric limb.

Figures 3 – 6 show that the line profiles appear in emission with a central reversal and broad, enhanced, asymmetric wings. However, the observed central reversals are not due to self-absorption by spicule plasma itself. The main characteristic of the self-absorption is that blue-shifted line core (the location of the central dip) produces a red asymmetry (higher red wing emission) and the red-shifted line core produces a blue asymmetry (higher blue wing emission). This is a well known phenomenon related to the shift in the wavelength of maximum opacity in the line core to shorter and longer wavelengths, which invokes the red and blue asymmetries, respectively (Kuridze et al. 2015b). The observed line profiles do not show this behavior suggesting that the central reversal could be due to strong opposite LoS velocity components within the spicule. The top part of the spicule at 08:38 and 08:41 UT has single peak line profiles without central reversal (Figures 5 and 6). Intensities at all wavelength positions across the Ca II line decrease as a function of height (Figures 3 – 6). The maximum line emission in the blue wing at around  $-0.7 \text{ \AA}$  from the line center drops by about a factor of  $\sim 3 - 10$  over the heights between  $\sim 2 - 9$  Mm above the limb (Figures 3 – 6).

#### 4. NICOLE INVERSION CODE AND SPICULE MODEL

##### 4.1. Modified version of NICOLE

NICOLE (Socas-Navarro et al. 2015) solves the multilevel non-LTE radiative transfer problem to invert or synthesize photospheric and chromospheric spectral lines (Socas-Navarro & Trujillo Bueno 1997). In the inversion mode the code iteratively perturbs physical parameters such as temperature, LoS velocity, magnetic field strength, and microturbulence in a predefined set of points (nodes) of an initial guess model atmosphere to find the best match with the observations (Socas-Navarro et al. 2000). We use here a five bound level-plus-continuum model of single ionized calcium atom with complete angle and frequency redistribution, which is applicable to lines such as Ca II  $8542 \text{ \AA}$  (Uitenbroek 1989).

As discussed above, NICOLE was not designed originally for inversions of spectra observed off the limb. A new version has been developed for this work with the following alterations. The model atmosphere may extend to heights of several Mm. The lower layers of the model up to 2 Mm represent the underlying average atmosphere and provide the radiation field illuminating the spicule from below. This lower part of the model is treated as before, except that it is kept fixed in the inversion. We chose the well-known Harvard-Smithsonian Reference Atmosphere model (HSRA; Gingerich et al. 1971) as a good representation of the average solar atmosphere.

The atmosphere above 2 Mm is identified with the spicule and will be the subject of our study. We initialize this upper part of the model with an extrapolation of HSRA. This model may be modified according to a number of free parameters that will be optimized by the code to provide the best fit to the observations in a least-squares sense. Motivated by the double-peak appearance of the profiles as well as some previous works in the literature, we decided to implement a two-component scenario. All the parameters that define the spicule model are duplicated (both components are, in principle, independent) and an additional parameter, the filling factor of each component, is introduced. This parameter is also height-dependent.

Each inversion iteration requires one or more calculations of synthetic profiles. The synthesis proceeds in two stages. In the first stage, an iteration scheme computes the atomic level populations that are self-consistent with the radiation field that they produce in this 1D model. The 1D approximation implies that each grid point sees the layers above and below as being infinite in the horizontal direction. This is a good approximation if the layers are optically thick because in this case one is not able to see the edge of the spicule. As we shall see below, this assumption is reasonably well justified.

We do not assume hydrostatic equilibrium in the spicule. The mass density is recovered as a smooth function interpolating between a set of nodes equispaced vertically along spicule axis. The number of nodes for the height-dependent variables is defined by the user.

The second stage computes the synthetic profiles with a final formal solution of the radiative transfer equation and convolves them with the CRISP transmission profile. In this case, the radiative transfer is solved in the horizontal

**Table 1.** Parameters of spicule model employed in the inversion.

Free parameters	
Temperature, $T$	1 node
Mass density <sup>a</sup> , $\rho$	3 nodes
LoS velocity, $V_{\text{LoS,red,blue}}$	3 nodes
Filling factor, $F_{\text{red,blue}}$	3 nodes
Fixed parameters	
Spicule thickness, $D$	1 000 km
Doppler width, $W_{\text{Dopp}}$	150 mÅ
Underlying atmosphere	HSRA

<sup>a</sup> – Electron density  $n_e$ , gas pressure  $p_{\text{gas}}$ , and electron pressure  $p_e$  are computed from the mass density  $\rho$  and the equation of state.

direction. The boundary condition for this transfer is that there is zero radiation field incoming from behind the spicule. We simply have to integrate at each height of interest in the direction perpendicular to the axis between the back of the spicule and the front. For this reason, the geometrical width of the spicule is relevant. It is a free parameter of the model (one for each component). The assumption of no incident radiation from behind the spicule is justified because the main body of the observed spicule is located above the chromospheric canopy and the forest of type II spicules. Therefore, there are no overlapping spicules along the LoS. Furthermore, the emission from the background and foreground corona and chromospheric canopy can be safely ignored as it has  $\sim 20 - 200$  times lower emission at  $\lambda = 8542 \text{ \AA}$  than the spicule itself in relevant heights, and these emissions were subtracted from the spicule spectra (Section 2.3).

#### 4.2. Double-component spicule model

The free parameters that characterize the model are the following. A user-defined number of nodes defines the height-dependent parameters: mass density  $\rho$ , line-of-sight velocity  $V_{\text{LoS}}$  and filling factor of the first component. The height-independent parameters are: temperature  $T$ , spicule thickness  $D$ , Doppler width  $W_{\text{Dopp}}$ .

Inspired by the double-peak appearance of Ca II profiles (Figures 3 – 6), we invoke a two-component spicule model, which represents separately the redshifted (red component) and blueshifted (blue component) lobes of spicule Ca II profiles by corresponding sets of height-dependent ( $\rho$ ,  $V_{\text{LoS}}$ ) and height-independent ( $T$ ,  $D$ ,  $W_{\text{Dopp}}$ ) parameters. With this scheme there are many free parameters. We sought to impose reasonable constraints on the model to reduce the degrees of freedom. Following the result by Beckers (1968), claiming that a model with constant temperature can reproduce the spicule intensities in chromospheric lines (see Section 6), we considered to start with the ansatz that spicules are isothermal features, even with the same temperature in both model components. We interpret the asymmetry in the peak intensities as due to different filling factors of the model components within a resolution element to represent different plasma volumes moving towards and away from an observer. As the peak intensity asymmetry varies with the height (Figures 3 – 6), we adopt height-dependent filling factors.

In order to constrain the model further, we impose that both components must have the same mass density stratification. Three nodes are used to define its height dependence  $\rho(z)$ . The stratifications of the electron density, electron and gas pressures are computed from the equation of state using the mass density obtained directly from inversions. We adopt three nodes for the LoS velocity of the blue model component  $V_{\text{LoS,blue}}$  and also three nodes for the LoS velocity of the red component  $V_{\text{LoS,red}}$ . It means it can vary as a second-order polynomial with height. We also assign three nodes for the height-dependent filling factors  $F_{\text{red}}, F_{\text{blue}}$  but constraining them by the condition  $F_{\text{red}} + F_{\text{blue}} = 1$ . Since the lower atmosphere (HSRA) is unchanged and the code only modifies the spicule model, the nodes are equispaced in the height scale  $z$  starting from  $z = 2 \text{ Mm}$ . Other parameters of the spicule model, such as spicule (i.e. segment) thickness  $D$  and Doppler width  $W_{\text{Dopp}}$  were fixed to the values shown in Table 1, which summarizes the model parameters and node numbers. Those values were found to be suitable choices after some manual exploration of the parameter space.

## 5. INVERSION RESULTS

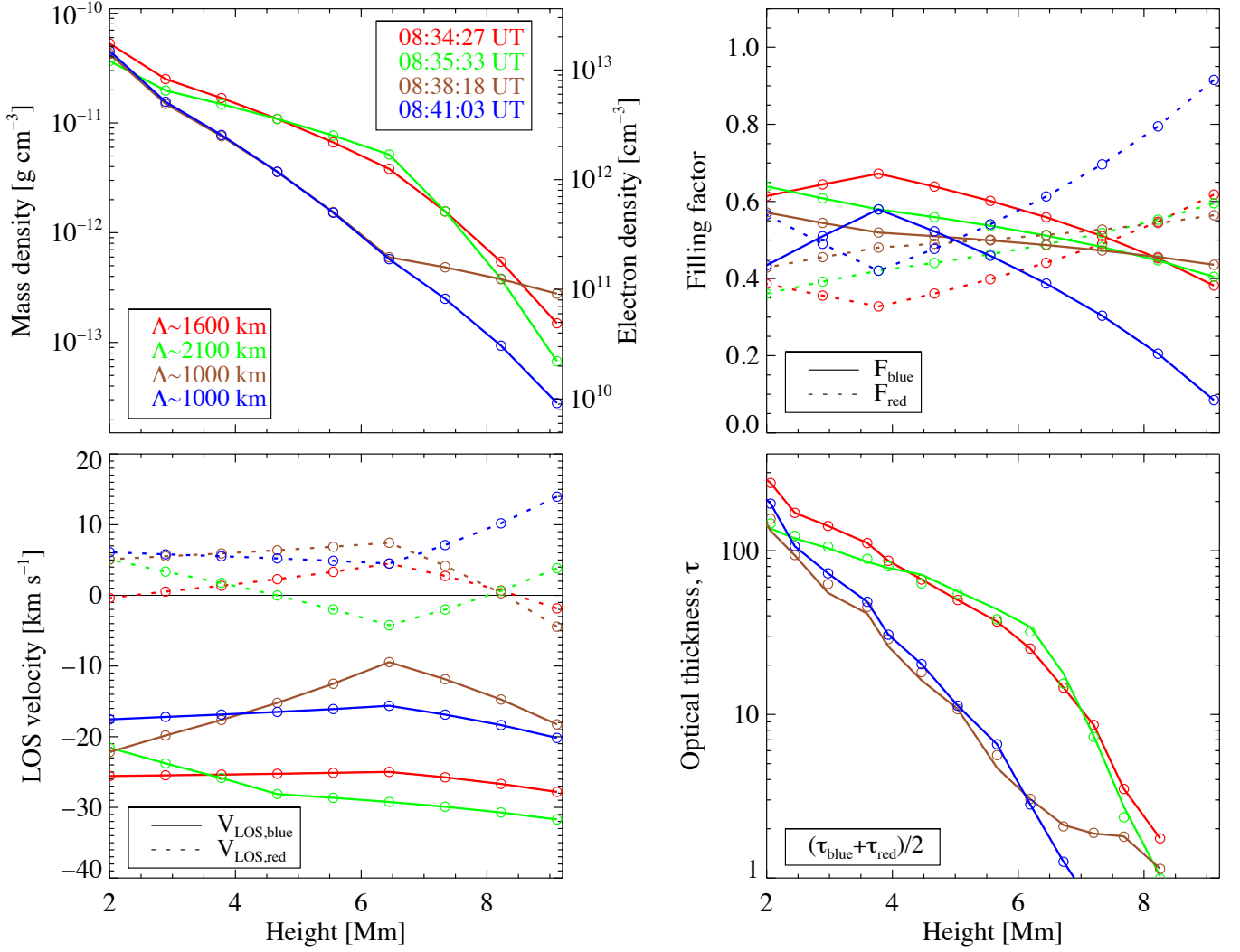


**Figure 7.** Height stratifications of parameters of the double-component spicule model inferred by the NICOLE inversion for the times shown in the right corner of the top left panel. Top left: The mass and electron densities (right  $y$  axis). Corresponding height scales  $\Lambda$  are shown in the bottom left corner. Bottom left and top right: The LoS velocities after compensating for the velocity of solar rotation and filling factors. Solid and dashed lines correspond to the blue and red component of the spicule model, respectively. Bottom right: The average optical thickness  $\tau$  in the Ca II 8542 Å line center as an average of the component optical thicknesses  $\tau_{\text{blue}}$  and  $\tau_{\text{red}}$ .

The new version of NICOLE fits simultaneously the observed Ca II profiles from fourteen different locations along the spicule axis with the double-component model that has a constant temperature and a smooth height-dependent density. The inversion is performed for four selected snapshots of the spicule lifetime. Figures 3 – 6 show the best-fit synthetic profiles resulting from the inversion. All models in the four selected snapshots characterize the constant temperature of  $T = 9560$  K in both components.

The height stratification of the mass density and the electron density, reproducing the fourteen observed Ca II profiles at four selected snapshots, are shown in Figure 7 (top left panel). In order to compute a density scale height, we fitted an exponential function (not shown) to the density stratifications retrieved by the inversion. The density scale heights  $\Lambda$  obtained in this manner are shown in the bottom left corner. The height scale drops from about 2100 km to about 1000 km over the interval of 7 minutes. The inversion yields the mass density of components typically in the range from about  $4 \times 10^{-11} \text{ g cm}^{-3}$  at the spicule bottom to about  $3 \times 10^{-14} \text{ g cm}^{-3}$  at its top. The corresponding electron densities computed from the mass densities by the equation of state are shown on the right  $y$  axis. They decrease from

about  $1.4 \times 10^{13} \text{ cm}^{-3}$  at the spicule bottom to about  $9 \times 10^9 \text{ cm}^{-3}$  at its top. The density drop in time is apparent especially in the upper parts of the spicule.

The variations of the LoS velocity in the blue ( $V_{\text{LoS,blue}}$ ) and red ( $V_{\text{LoS,red}}$ ) components of the spicule model are shown in the bottom left panel of Figure 7. Disregarding the height-time variations, we can take  $-22 \text{ km s}^{-1}$  as typical for the former and  $+3 \text{ km s}^{-1}$  for the latter. We interpret the asymmetry in their absolute values as a consequence of vector superposition of counter-oriented Doppler velocity components of spicule tilted toward the observers. The whole-spicule decrease of  $|V_{\text{LoS,blue}}|$  from about  $27 \text{ km s}^{-1}$  to  $16 \text{ km s}^{-1}$  is followed by an increase of  $|V_{\text{LoS,red}}|$  from about  $1 \text{ km s}^{-1}$  to  $6 \text{ km s}^{-1}$  apparent below  $\sim 6 \text{ Mm}$ . This is compatible with the ceasing of upflow motion and also with the drop of density scale height  $\Lambda$  over time.

The top right panel of Figure 7 shows height-time variations of the filling factor in the blue ( $F_{\text{blue}}$ ) and red ( $F_{\text{red}}$ ) component of the spicule model. It suggests roughly balanced  $\sim 50/50$  coverage of the resolution element by the spicule model components at all heights. An exception is the last moment (08:41:03 UT) shown in blue, when the red model component ( $F_{\text{red}}$ ) dominates over the resolution element at the heights above  $\sim 7 \text{ Mm}$ .

The bottom right panel of Figure 7 shows the average optical thickness of spicule  $\tau$  in the Ca II line center. Due to the same mass densities of both model components, the component optical thicknesses  $\tau_{\text{blue}}$  and  $\tau_{\text{red}}$  are also almost the same. Therefore the panel shows their simple average separately for the four selected times. The optical thickness decreases exponentially from about 300 at the spicule bottom to about one at its top. It proves that the spicule plasma is mostly optically thick in Ca II and validates our assumption about infinitely extended plane-parallel spicule slab in the radiative transfer calculations (Section 4.1). The drop of  $\tau$  over time in its upper part is also apparent.

We note that, the inversions can not achieve a good fit at the top part of the spicule (Figures 3 – 6, points 13 – 14). Due to the significant change in relative amplitudes of the two components at the top, the code can not fit the line profiles with the same success using the same parametrisation. The ratio of amplitudes along the spicule is nearly constant but at the top one component vanishes and the ratio raises significantly. Possible reason could be the end of the helical structure or spinning/unwinding motion, when the field does not wrap around any more at the top part of the spicule. We plan to explore this in more detail in the follow up paper where we use the 2D models.

### 5.1. Response functions

To investigate the sensitivity and response of the Stokes  $I$  Ca II profiles to variations of physical parameters, we investigate the numerical response functions (RFs) for the spicule model implemented in the new version of NICOLE. The response function  $RF_x(\lambda)$  to the given atmospheric parameter  $x$  is a measure of how the line intensity at a given wavelength  $\lambda$  reacts to a small perturbation on  $x$ . Formally,  $RF_x(\lambda)$  to the parameter  $x$  is defined as:

$$RF_x(\lambda) = [I_{\text{pert}}(\lambda) - I_{\text{ref}}(\lambda)] / (x_{\text{pert}} - x_{\text{ref}}), \quad (1)$$

where  $x_{\text{ref}}$  is a reference value of a spicule model parameter producing reference intensity  $I_{\text{ref}}(\lambda)$  at  $\lambda$  and  $x_{\text{pert}}$  is the value of perturbed parameter producing the perturbed intensity  $I_{\text{pert}}(\lambda)$ . In the limit when  $x_{\text{pert}}$  tends to  $x$ , the expression becomes the mathematical representation of a derivative. Figure 8 shows the Stokes  $I$  RFs of the Ca II line to perturbations of the temperature, spicule thickness, and mass density for the fourteen segments of the blue component of the spicule model. The curves are normalized to maximum values of corresponding  $RF_x$ . All displayed RFs show maxima or minima at  $\Delta\lambda \sim -0.6 \text{ \AA}$ . While the RFs suggest different response of Ca II blue wing intensity to parameter perturbations in the bottom spicule segments 1 – 6 there is a strong degeneracy of response in most of the upper segments 6 – 14 — the blue wing intensity reacts the same to parameter perturbations of the blue component model of spicule. This is the reason why it would not be possible to invert each spectrum separately. One needs the constraints given by a consistent height-dependent model to fit all the observations at various heights.

## 6. DISCUSSION AND CONCLUSIONS

We study an off-limb solar spicule using high-resolution imaging spectroscopy obtained in the Ca II 8542  $\text{\AA}$  line by the SST/CRISP instrument. We use a new version of the non-LTE code NICOLE assuming a double-component spicule model to infer the spicule temperature and height stratifications of density, and LoS velocity along the spicule axis defined by pixel positions at the maxima of line integrated intensities.

Our analyses shows that the spicule plasma is isothermal having the uniform temperature of 9560 K along its length in the time interval of 7 minutes. Early and also recent measurements reported temperature variation along the spicule axis (Beckers 1968, 1972; Alissandrakis 1973; Krall et al. 1976; Matsuno & Hirayama 1988; Alissandrakis et al. 2018).

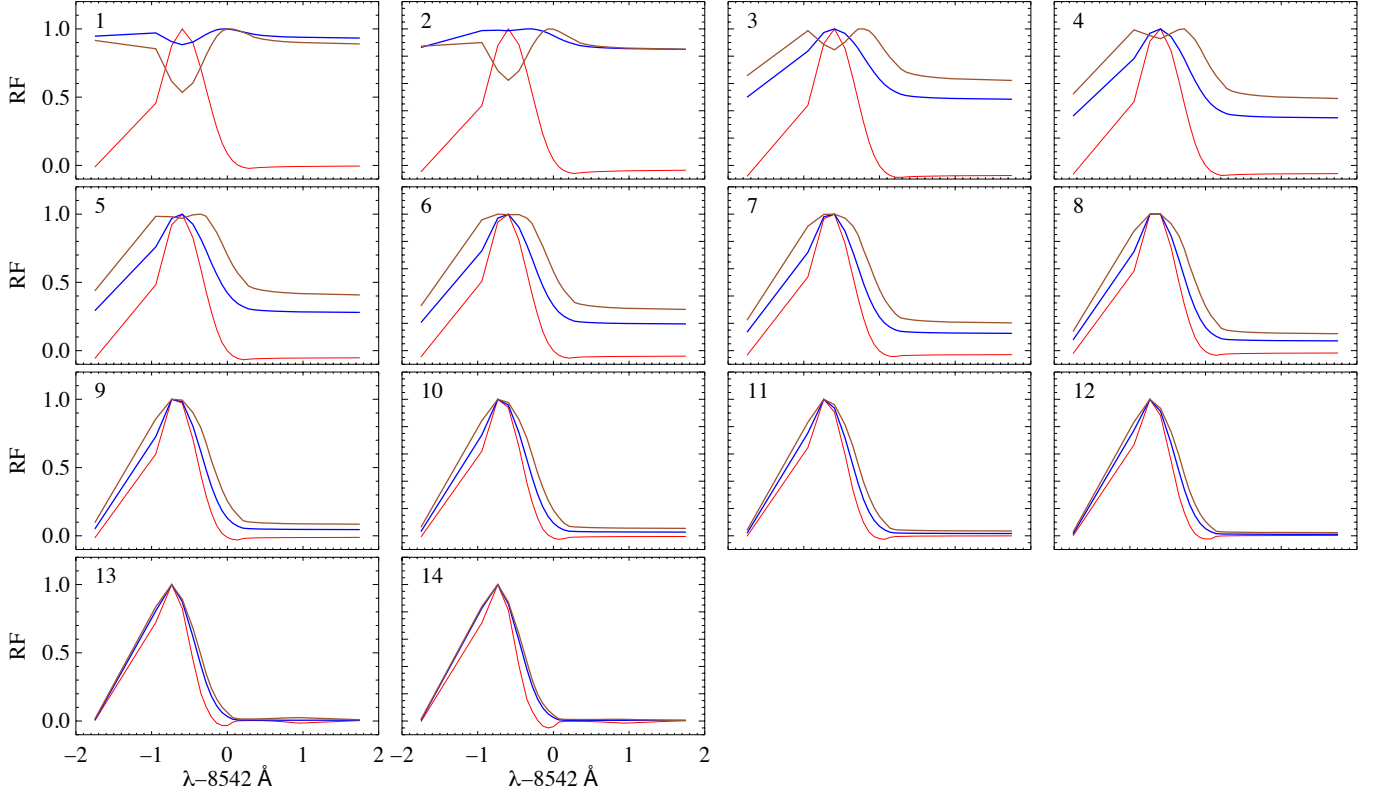


**Figure 8.** Numerical Stokes  $I$  response functions of the Ca II 8542 Å line for temperature (red), spicule thickness (brown), and mass density (blue) for the blue component of spicule model normalized to their maximum values.

However, despite being reported some temperature variations, based on analyses of the  $T_e - n_e$  curves at different heights, the pioneering work of [Beckers \(1968\)](#) concluded that the spicule intensities in chromospheric lines do not yield information about temperature variation and hence observed spectral characteristics in principle can be reproduced by a spicule model with uniform temperature (see page 408 therein). In this context [Krall et al. \(1976\)](#) also mentioned that H $\alpha$  emission is a rather sensitive indicator of electron density and relatively independent of temperature over a large temperature range (see page 100 therein). Our results confirms this as we fitted multiple Ca II profiles with constant temperature in four selected snapshots from the spicule lifetime. The inverted Y-shaped topology of the spicule footpoint implies a magnetic reconnection in the junction point that may have populated the spicule body with plasma of uniform temperature.

As shown in Figure 7 the mass and electron densities of the spicule plasma decrease exponentially as a function of height. We note that the analysed structure bears many similarities and dissimilarities with conventional spicules making its unequivocal classification substantially difficult within current taxonomy of diverse small-scale jets. The structure has a similar width, length and line profiles to the spicules analysed in [Beckers \(1968, 1972\)](#), providing the main motivation to interpret it as spicule. However, density obtained through the inversion makes this structure more similar to the larger scale chromospheric jets (macrospicule/surges) rather than typical spicules. The values of the electron density  $n_e$  at four different times near the base of the spicule at a height of  $z \sim 2$  Mm is around  $10^{13} \text{ cm}^{-3}$ . [Beckers \(1972\)](#) derived  $n_e \sim 1.6 \times 10^{11} \text{ cm}^{-3}$  at height of  $z \sim 2$  Mm, around 60 times less than our estimates. Furthermore, [Beckers \(1972\)](#) estimates that  $n_e$  decreases by 20 times at the top of the spicule at height of  $\sim 10$  Mm, whereas our models show that the mass and electron densities decrease by  $\sim 100$  times at height of  $z \sim 9$  Mm for the first three models (Figure 7: top left panel). The model at a late phase of the spicule (at 08:41 UT, around 2 min before the disappearance) shows a sharper drop in density and pressure. [Alissandrakis \(1973\)](#) performed multiline spectroscopy of 36 spicules and found that the average values of the electron density at a height of 5 400 km is around  $6 \times 10^{10} \text{ cm}^{-3}$ . Our models show that the  $n_e$  at the same height varies between  $1 - 3 \times 10^{12} \text{ cm}^{-3}$  for the four different models (Figure 7: top left panel).



The density and pressure scale heights of spicules measured from our diagnostics are in the range of  $\Lambda \sim 1000 - 2100$  km over the  $\sim 2 - 9$  Mm length projected to the surface normal (Figure 7: top left panel). This is higher than some previous estimates of the scale heights in limb spicules using eclipse flash spectra (Makita 2003) and magneto-seismology (Verth et al. 2011). Density scale heights derived by Bjølseth (2008) from Ca II H intensities in spicules vary between  $\sim 2 - 8$  Mm (see Figure 4.10 of Bjølseth (2008)). However, Bjølseth (2008) assumes that the source function is constant along the spicule, and hence the scale height of the intensity is defined only by the density stratification. In our case, the wavelength-integrated Ca II intensities (not shown) decrease by a factor of  $\sim 10 - 16$  in the range  $2 - 8$  Mm along the spicule, much slower than density and pressure (Figure 7: top left panel). Estimated density/pressure scale heights are also much higher than the scale height of  $\sim 290$  km of gas with comparable temperature in hydrostatic equilibrium. This is not surprising as the observed spicule displays a complex dynamic behavior during its lifetime. Inversions distinguish two LoS velocity components along the spicule.

The double-peak Ca II 8542 Å profiles detected along the jet axis are likely due to the unwinding of highly twisted field lines rooted in magnetic topology with opposite polarities. Unwinding twists can appear as a spinning motion of the plasma strands as found in rotating chromospheric jets (see e.g., Shibata & Uchida 1986; Canfield et al. 1996; Liu et al. 2009, 2011; Pariat et al. 2015). The line-of-sight superposition of such strands may result in the double-peak profiles observed along the jet axis. Liu et al. (2009) has shown the observations of reconnection-driven jet, which involves untwisting helical threads rotating about the axis of a single large cylinder and shedding magnetic helicity into the upper atmosphere. They proposed the model in which flux emergence in an open-field region leads to magnetic reconnection, forming a jet and fan-spine topology. The twists in the reconnected open field tend to unwind themselves and drive these field lines to rotate (Liu et al. 2011). The spicule analysed in this paper resembles much the fan-spine magnetic reconnection topology resulting from flux emergence studied in Liu et al. (2011) and displays a spinning motion during its lifetime.

We note that the bi-directional flows along the spicular jet with parallel field lines in unipolar topology can also produce centrally reversed profiles of spicules. An observation of bi-directional flows at tops and bases of spicules is reported in Pasachoff et al. (2009). Signature of counterstreams along a simulated macrospicule can be found in Murawski et al. (2011) for vertical or oblique magnetic field. However, Murawski et al. (2011) consider a localized velocity pulse as a driver of macrospicule, whereas the Y-shaped base of the spicule analysed in this study suggests the magnetic reconnection for the formation mechanism (Figure 1). Furthermore, there is no clear and obvious evidence of the bi-directional flows in the observed spicule. Therefore, double-peak profiles of the spicule presented in this study is less likely to be a manifestation of counterstreaming or bi-directional flow.

The fact that the two spicule components have different amplitudes of the maximum intensity could be due to the different filling factors within a resolution element. Indeed, inversions with height-dependent filling factors for red and blue components provided the best fit with the observations. The exact relation of the spicule spectra with the dynamic motion and its transverse structure will be studied in a future paper where we plan to perform full 2D analysis and inversions of our observations.

The optical thickness  $\tau$  in the Ca II line center, i.e. where opacity reaches maximum, is a few hundreds at the spicule bottom and decreases exponentially toward its top. Over the main part of the spicule the  $\tau$  is well above one, thus classifying the spicule plasma as optically thick in the Ca II line center. Krall et al. (1976) performed theoretical calculations of the spicule optical thickness  $\tau_{8542}$  in the Ca II line center for the temperatures and electron densities ranging from 10 000 K to 20 000 K and from  $2 \times 10^{10} \text{ cm}^{-3}$  to  $1 \times 10^{11} \text{ cm}^{-3}$ , respectively, but inferring  $\tau_{8542}$  mostly of the order of  $1 \times 10^{-2} - 1 \times 10^{-3}$ . They assumed the spicule thickness of 1 425 km (see page 100 therein), thus larger than the thickness of 1 000 km employed here (Table 1). The high optical thickness could be related to the measured high density of spicule along its length.

We note that there are only limited number of radiative transfer codes that can deal with the off-limb emissions of the structures such as spicules. One of the most advanced is non-LTE inversion code HAZEL (Asensio Ramos et al. 2008), which may be of interest for other similar investigations. We have decided to employ NICOLE for this work because of some unique features that are very important in this context, such as the ability to calculate Ca II populations in an optically thick medium with radiative transfer.

Generally, the main problem of inversion techniques is the possible non-uniqueness of the obtained solutions due to the degeneracy between the different parameters. We have investigated the degeneracy between temperature, density, and thickness of the spicule in the models obtained through inversion by analyzing the response functions of the intensity to the perturbations of these parameters. The results presented in Figure 8 indicate that profiles 8 to 14 have

a strong degeneracy among the three parameters. This means that we could obtain exactly the same solution with different combinations of those three parameters. Therefore, if we were fitting those profiles individually, we would have no way to obtain a unique solution. However, the degeneracy is broken as the response functions are not the same for the profiles of the bottom and middle parts of the spicule (see profiles 1 to 7 in Figure 8). As long as we fit all of the profiles simultaneously the models obtained are free of this degeneracy and the results are reasonably reliable.

We note that the spectral diagnostics presented here are applicable to the local plasma parameters of a particular spicule and they may not necessarily be considered as typical of all spicular structures. However, it has been demonstrated that inversions can be successfully applied to spicule spectra at multiple height positions. With a wealth of statistics of semi-empirical spicule models, we might gain a better understanding of chromospheric spicules, their properties, and dynamics.

To our knowledge, this is the first spectral diagnostics of the physical parameters of a spicule through line profile fitting with a non-LTE inversion code. The results are very encouraging for future semi-empirical modeling of spicules using inversion techniques and high-resolution spectropolarimetric observations with present and future ground-based observing facilities.

### ACKNOWLEDGMENTS

The research leading to these results has received funding from the Sêr Cymru II scheme, part-funded by the European Regional Development Fund through the Welsh Government, and STFC grant ST/S000518/1 to Aberystwyth University. The work of D.K. was supported by Georgian Shota Rustaveli National Science Foundation project FR17\_323. H.S.N. acknowledges support from the Spanish Ministry of Economy and Competitiveness through project AYA2014-60476-P and PGC2018-102108-B-I00. The Swedish 1-m Solar Telescope is operated on the island of La Palma by the Institute for Solar Physics of Stockholm University in the Spanish Observatorio del Roque de los Muchachos of the Instituto de Astrofísica de Canarias. The Institute for Solar Physics is supported by a grant for research infrastructures of national importance from the Swedish Research Council (registration number 2017-00625). J.K. acknowledges the project VEGA 2/0048/20. R.O. acknowledges support from the Spanish Ministry of Economy and Competitiveness (MINECO) and FEDER funds through project AYA2017-85465-P. Ellie Nicholson is gratefully acknowledged for language corrections.

*Facility:* SST(CRISP), NICOLE

### REFERENCES

- Alissandrakis, C. E. 1973, *SoPh*, 32, 345, doi: [10.1007/BF00154947](https://doi.org/10.1007/BF00154947)
- Alissandrakis, C. E., Tsiropoula, G., & Mein, P. 1990, *A&A*, 230, 200
- Alissandrakis, C. E., Vial, J. C., Koukras, A., Büchlin, E., & Chane-Yook, M. 2018, *SoPh*, 293, 20, doi: [10.1007/s11207-018-1242-4](https://doi.org/10.1007/s11207-018-1242-4)
- Asensio Ramos, A., Trujillo Bueno, J., & Landi Degl’Innocenti, E. 2008, *ApJ*, 683, 542, doi: [10.1086/589433](https://doi.org/10.1086/589433)
- Beck, C., Rezaei, R., Puschmann, K. G., & Fabbian, D. 2016, *SoPh*, 291, 2281
- Beckers, J. M. 1964, *ApJ*, 140, 1339, doi: [10.1086/148038](https://doi.org/10.1086/148038)
- . 1968, *SoPh*, 3, 367, doi: [10.1007/BF00171614](https://doi.org/10.1007/BF00171614)
- . 1972, *ARA&A*, 10, 73, doi: [10.1146/annurev.aa.10.090172.000445](https://doi.org/10.1146/annurev.aa.10.090172.000445)
- Bjølseth, S. 2008, Masters thesis, Univ. Oslo
- Canfield, R. C., Reardon, K. P., Leka, K. D., et al. 1996, *ApJ*, 464, 1016, doi: [10.1086/177389](https://doi.org/10.1086/177389)
- Cauzzi, G., Reardon, K. P., Uitenbroek, H., et al. 2008, *A&A*, 480, 515, doi: [10.1051/0004-6361:20078642](https://doi.org/10.1051/0004-6361:20078642)
- Centeno, R., Trujillo Bueno, J., & Asensio Ramos, A. 2010, *ApJ*, 708, 1579, doi: [10.1088/0004-637X/708/2/1579](https://doi.org/10.1088/0004-637X/708/2/1579)
- de la Cruz Rodríguez, J., Hansteen, V., Bellot-Rubio, L., & Ortiz, A. 2015, *ApJ*, 810, 145, doi: [10.1088/0004-637X/810/2/145](https://doi.org/10.1088/0004-637X/810/2/145)
- de la Cruz Rodríguez, J., Löfdahl, M. G., Sütterlin, P., Hillberg, T., & Rouppe van der Voort, L. 2015, *A&A*, 573, A40, doi: [10.1051/0004-6361/201424319](https://doi.org/10.1051/0004-6361/201424319)
- de la Cruz Rodríguez, J., Rouppe van der Voort, L., Socas-Navarro, H., & van Noort, M. 2013, *A&A*, 556, A115, doi: [10.1051/0004-6361/201321629](https://doi.org/10.1051/0004-6361/201321629)
- de la Cruz Rodríguez, J., & van Noort, M. 2017, *SSRv*, 210, 109, doi: [10.1007/s11214-016-0294-8](https://doi.org/10.1007/s11214-016-0294-8)

- De Pontieu, B., Erdélyi, R., & James, S. P. 2004, *Nature*, 430, 536, doi: [10.1038/nature02749](https://doi.org/10.1038/nature02749)
- de Pontieu, B., McIntosh, S., Hansteen, V. H., et al. 2007, *PASJ*, 59, S655, doi: [10.1093/pasj/59.sp3.S655](https://doi.org/10.1093/pasj/59.sp3.S655)
- De Pontieu, B., Title, A. M., Lemen, J. R., et al. 2014, *SoPh*, 289, 2733, doi: [10.1007/s11207-014-0485-y](https://doi.org/10.1007/s11207-014-0485-y)
- Gingerich, O., Noyes, R. W., Kalkofen, W., & Cuny, Y. 1971, *SoPh*, 18, 347, doi: [10.1007/BF00149057](https://doi.org/10.1007/BF00149057)
- Hansteen, V. H., De Pontieu, B., Rouppe van der Voort, L., van Noort, M., & Carlsson, M. 2006, *ApJL*, 647, L73, doi: [10.1086/507452](https://doi.org/10.1086/507452)
- He, J., Marsch, E., Tu, C., & Tian, H. 2009, *ApJL*, 705, L217, doi: [10.1088/0004-637X/705/2/L217](https://doi.org/10.1088/0004-637X/705/2/L217)
- Krall, K. R., Bessey, R. J., & Beckers, J. M. 1976, *SoPh*, 46, 93, doi: [10.1007/BF00157556](https://doi.org/10.1007/BF00157556)
- Kriginsky, M., Oliver, R., Freij, N., et al. 2020, *A&A*, 642, A61, doi: [10.1051/0004-6361/202038546](https://doi.org/10.1051/0004-6361/202038546)
- Kuridze, D., Henriques, V., Mathioudakis, M., et al. 2015a, *ApJ*, 802, 26, doi: [10.1088/0004-637X/802/1/26](https://doi.org/10.1088/0004-637X/802/1/26)
- . 2017, *ApJ*, 846, 9, doi: [10.3847/1538-4357/aa83b9](https://doi.org/10.3847/1538-4357/aa83b9)
- Kuridze, D., Henriques, V. M. J., Mathioudakis, M., et al. 2018, *ApJ*, 860, 10, doi: [10.3847/1538-4357/aac26d](https://doi.org/10.3847/1538-4357/aac26d)
- Kuridze, D., Verth, G., Mathioudakis, M., et al. 2013, *ApJ*, 779, 82, doi: [10.1088/0004-637X/779/1/82](https://doi.org/10.1088/0004-637X/779/1/82)
- Kuridze, D., Mathioudakis, M., Simões, P. J. A., et al. 2015b, *ApJ*, 813, 125, doi: [10.1088/0004-637X/813/2/125](https://doi.org/10.1088/0004-637X/813/2/125)
- Langangen, Ø., De Pontieu, B., Carlsson, M., et al. 2008, *ApJL*, 679, L167, doi: [10.1086/589442](https://doi.org/10.1086/589442)
- Linsky, J. L., Teske, R. G., & Wilkinson, C. W. 1970, *SoPh*, 11, 374, doi: [10.1007/BF00153072](https://doi.org/10.1007/BF00153072)
- Lites, B. W. 1983, *SoPh*, 85, 193, doi: [10.1007/BF00148648](https://doi.org/10.1007/BF00148648)
- Liu, W., Berger, T. E., Title, A. M., & Tarbell, T. D. 2009, *ApJL*, 707, L37, doi: [10.1088/0004-637X/707/1/L37](https://doi.org/10.1088/0004-637X/707/1/L37)
- Liu, W., Berger, T. E., Title, A. M., Tarbell, T. D., & Low, B. C. 2011, *ApJ*, 728, 103, doi: [10.1088/0004-637X/728/2/103](https://doi.org/10.1088/0004-637X/728/2/103)
- Löfdahl, M. G. 2002, in *Society of Photo-Optical Instrumentation Engineers (SPIE) Conference Series*, Vol. 4792, *Image Reconstruction from Incomplete Data*, ed. P. J. Bones, M. A. Fiddy, & R. P. Millane, 146–155, doi: [10.1117/12.451791](https://doi.org/10.1117/12.451791)
- Löfdahl, M. G., Hillberg, T., de la Cruz Rodriguez, J., et al. 2018, *ArXiv e-prints*. <https://arxiv.org/abs/1804.03030>
- López Ariste, A., & Casini, R. 2005, *A&A*, 436, 325, doi: [10.1051/0004-6361:20042214](https://doi.org/10.1051/0004-6361:20042214)
- Makita, M. 2003, *Publications of the National Astronomical Observatory of Japan*, 7, 1
- Matsuno, K., & Hirayama, T. 1988, *SoPh*, 117, 21, doi: [10.1007/BF00148569](https://doi.org/10.1007/BF00148569)
- Morita, S., Shibata, K., UeNo, S., et al. 2010, *PASJ*, 62, 901, doi: [10.1093/pasj/62.4.901](https://doi.org/10.1093/pasj/62.4.901)
- Morton, R. J. 2014, *A&A*, 566, A90, doi: [10.1051/0004-6361/201423718](https://doi.org/10.1051/0004-6361/201423718)
- Murawski, K., Srivastava, A. K., & Zaqarashvili, T. V. 2011, *A&A*, 535, A58, doi: [10.1051/0004-6361/201117589](https://doi.org/10.1051/0004-6361/201117589)
- Nelson, C. J., Freij, N., Bennett, S., Erdélyi, R., & Mathioudakis, M. 2019, *ApJ*, 883, 115, doi: [10.3847/1538-4357/ab3a54](https://doi.org/10.3847/1538-4357/ab3a54)
- Nishizuka, N., Nakamura, T., Kawate, T., Singh, K. A. P., & Shibata, K. 2011, *ApJ*, 731, 43, doi: [10.1088/0004-637X/731/1/43](https://doi.org/10.1088/0004-637X/731/1/43)
- Orozco Suárez, D., Asensio Ramos, A., & Trujillo Bueno, J. 2015, *ApJL*, 803, L18, doi: [10.1088/2041-8205/803/2/L18](https://doi.org/10.1088/2041-8205/803/2/L18)
- Pariat, E., Dalmasse, K., DeVore, C. R., Antiochos, S. K., & Karpen, J. T. 2015, *A&A*, 573, A130, doi: [10.1051/0004-6361/201424209](https://doi.org/10.1051/0004-6361/201424209)
- Pasachoff, J. M., Jacobson, W. A., & Sterling, A. C. 2009, *SoPh*, 260, 59, doi: [10.1007/s11207-009-9430-x](https://doi.org/10.1007/s11207-009-9430-x)
- Pereira, T. M. D., De Pontieu, B., Carlsson, M., et al. 2014, *ApJL*, 792, L15, doi: [10.1088/2041-8205/792/1/L15](https://doi.org/10.1088/2041-8205/792/1/L15)
- Pietarila, A., Socas-Navarro, H., & Bogdan, T. 2007, *ApJ*, 663, 1386, doi: [10.1086/518714](https://doi.org/10.1086/518714)
- Ramelli, R., Bianda, M., Merenda, L., & Trujillo Bueno, T. 2006, in *Astronomical Society of the Pacific Conference Series*, Vol. 358, *Solar Polarization 4*, ed. R. Casini & B. W. Lites, 448
- Ramelli, R., Bianda, M., Trujillo Bueno, J., Merenda, L., & Stenflo, J. O. 2005, in *ESA Special Publication*, Vol. 596, *Chromospheric and Coronal Magnetic Fields*, ed. D. E. Innes, A. Lagg, & S. A. Solanki, 82.1
- Rouppe van der Voort, L., Leenaarts, J., de Pontieu, B., Carlsson, M., & Vissers, G. 2009, *ApJ*, 705, 272, doi: [10.1088/0004-637X/705/1/272](https://doi.org/10.1088/0004-637X/705/1/272)
- Scharmer, G. B. 2006, *A&A*, 447, 1111, doi: [10.1051/0004-6361:20052981](https://doi.org/10.1051/0004-6361:20052981)
- Scharmer, G. B., Narayan, G., Hillberg, T., et al. 2008, *ApJL*, 689, L69, doi: [10.1086/595744](https://doi.org/10.1086/595744)
- Secchi, A. 1875, *Le Soleil* (Gauthier-Villars, Paris), doi: [10.3931/e-rara-14748](https://doi.org/10.3931/e-rara-14748)
- Shibata, K., & Uchida, Y. 1986, *SoPh*, 103, 299, doi: [10.1007/BF00147831](https://doi.org/10.1007/BF00147831)
- Shibata, K., Nakamura, T., Matsumoto, T., et al. 2007, *Science*, 318, 1591, doi: [10.1126/science.1146708](https://doi.org/10.1126/science.1146708)
- Shimojo, M., Kawate, T., Okamoto, T. J., et al. 2020, *ApJL*, 888, L28, doi: [10.3847/2041-8213/ab62a5](https://doi.org/10.3847/2041-8213/ab62a5)
- Skogsrud, H., Rouppe van der Voort, L., De Pontieu, B., & Pereira, T. M. D. 2015, *ApJ*, 806, 170, doi: [10.1088/0004-637X/806/2/170](https://doi.org/10.1088/0004-637X/806/2/170)

- Socas-Navarro, H., de la Cruz Rodríguez, J., Asensio Ramos, A., Trujillo Bueno, J., & Ruiz Cobo, B. 2015, *A&A*, 577, A7, doi: [10.1051/0004-6361/201424860](https://doi.org/10.1051/0004-6361/201424860)
- Socas-Navarro, H., & Elmore, D. 2005, *ApJL*, 619, L195, doi: [10.1086/428399](https://doi.org/10.1086/428399)
- Socas-Navarro, H., & Trujillo Bueno, J. 1997, *ApJ*, 490, 383, doi: [10.1086/304873](https://doi.org/10.1086/304873)
- Socas-Navarro, H., Trujillo Bueno, J., & Ruiz Cobo, B. 2000, *ApJ*, 530, 977, doi: [10.1086/308414](https://doi.org/10.1086/308414)
- Sterling, A. C. 2000, *SoPh*, 196, 79, doi: [10.1023/A:1005213923962](https://doi.org/10.1023/A:1005213923962)
- Suematsu, Y., Wang, H., & Zirin, H. 1995, *ApJ*, 450, 411, doi: [10.1086/176151](https://doi.org/10.1086/176151)
- Tei, A., Gunár, S., Heinzel, P., et al. 2020, *ApJ*, 888, 42, doi: [10.3847/1538-4357/ab5db1](https://doi.org/10.3847/1538-4357/ab5db1)
- Trujillo Bueno, J. 2010, *Astrophysics and Space Science Proceedings*, 19, 118, doi: [10.1007/978-3-642-02859-5\\_9](https://doi.org/10.1007/978-3-642-02859-5_9)
- Trujillo Bueno, J., Merenda, L., Centeno, R., Collados, M., & Landi Degl’Innocenti, E. 2005, *ApJL*, 619, L191, doi: [10.1086/428124](https://doi.org/10.1086/428124)
- Tsiropoula, G., & Schmieder, B. 1997, *A&A*, 324, 1183
- Tsiropoula, G., Tziotziou, K., Kontogiannis, I., et al. 2012, *SSRv*, 169, 181, doi: [10.1007/s11214-012-9920-2](https://doi.org/10.1007/s11214-012-9920-2)
- Tziotziou, K., Tsiropoula, G., & Mein, P. 2003, *A&A*, 402, 361, doi: [10.1051/0004-6361:20030220](https://doi.org/10.1051/0004-6361:20030220)
- Uitenbroek, H. 1989, *A&A*, 213, 360
- van Noort, M., Rouppe van der Voort, L., & Löfdahl, M. G. 2005, *SoPh*, 228, 191, doi: [10.1007/s11207-005-5782-z](https://doi.org/10.1007/s11207-005-5782-z)
- Verth, G., Goossens, M., & He, J. S. 2011, *ApJL*, 733, L15, doi: [10.1088/2041-8205/733/1/L15](https://doi.org/10.1088/2041-8205/733/1/L15)
- Wootten, A., & Thompson, A. R. 2009, *IEEE Proceedings*, 97, 1463, doi: [10.1109/JPROC.2009.2020572](https://doi.org/10.1109/JPROC.2009.2020572)
- Yokoyama, T., & Shibata, K. 1995, *Nature*, 375, 42, doi: [10.1038/375042a0](https://doi.org/10.1038/375042a0)
- Zaqarashvili, T. V., & Erdélyi, R. 2009, *SSRv*, 149, 355, doi: [10.1007/s11214-009-9549-y](https://doi.org/10.1007/s11214-009-9549-y)
- Zaqarashvili, T. V., Khutsishvili, E., Kukhianidze, V., & Ramishvili, G. 2007, *A&A*, 474, 627, doi: [10.1051/0004-6361:20077661](https://doi.org/10.1051/0004-6361:20077661)